4 From Kirchhoff Prestack Depth Migration to Fresnel Volume Migration

With the rapid enhancement of computing power and the refinement of the algorithms in the last three decades, migration of reflection seismic data became more and more popular to image the subsurface. Thereby, the final goal is to obtain detailed images of the geological and tectonic structures in the subsurface by repositioning the measured reflections and diffractions to their correct position at depth.

Two different approaches to implement migration are generally used: A kinematic scheme based on ray theory or a dynamic migration procedure based on wave theory. The latter consists of two steps. Firstly, a back propagation of the recorded wavefield in time down into the subsurface has to be done. Secondly, as the actual imaging step, the seismic energy has to be placed at the subsurface point at the travel time from the source to this subsurface point.

For wavefield back propagation, three main techniques are differentiated and all of them are commonly used in practice (e.g. Sheriff & Geldart, 1995). The genus of frequency-wavenumber migration involves techniques such as Fourier transform migration (e.g. Stolt, 1978) and phase-shift migration (Gazdag, 1978; Gazdag & Squazzero, 1984) depending on whether they work in the frequency-offset domain or in the f-k domain. The disadvantages of the latter methods are, that some of them are either unable to handle lateral velocity variations or they are computationally expensive (e.g. Guo & Fagin, 2002). Claerbout (1976) made the pioneer work with numerical finite-difference (FD) solutions of the wave equation. This method is commonly known as the finite-difference method of wave equation migration. In this thesis the the Kirchhoff method, based on an integral solution of the wave equation (Schneider, 1978), was used.

As an extention of Kirchhoff Prestack Depth Migration, a new approach was implemented in order to improve the images. This so-called *Fresnel Volume Migration* is based on the restriction of the migration operator to enhance that portion of the signal which physically contributes to a reflection event within the migration scheme.

The idea to limit the operator in such a way is not new. Several methods to solve this problem have been investigated in the past, especially with the aim to overcome problems with migration artifacts due to a limited aperture. Most of these applications work with information about the wave direction when it reaches the receivers. The slowness-weighted diffraction stack, firstly presented by Milkereit (1987a), was only applied to wide-angle data by Van Avendonk (2004) until now. Another restriction method is given by the Gaussian beam migration (Hill, 1990; Gray, 2005) where the amplitudes are summed within a downward propagated Gaussian beam which broadens with increasing depth. A similar approach to the Fresnel Volume Migration, the wavepath migration, was proposed by Sun & Schuster (2001, 2003). In contrast to Fresnel Volume Migration, they worked with additional approximations which are: the use of a ray tracing algorithm which is part of a general seismic inversion technique for travel time estimation and the application of a slant stack to smear amplitudes of more than one trace along the same wavepath.

The first three sections of this chapter outline an overview of the Kirchhoff Prestack Depth Migration procedure as well as a detailed discussion of the influence of the velocity information to the migration results. A detailed insight into the Kirchhoff migration scheme and the integral solution of the wave equation is given by Schneider (1978), Müller (1997) and Schleicher *et al.* (1993). The extension of Kirchhoff Prestack Depth Migration to Fresnel Volume Migration including the corresponding preparatory work is described in the sections 4.4 - 4.6. A number of modelling studies with respect to Fresnel Volume Migration can be found in Lüth *et al.* (2005) and Heigel (2005).

4.1 Kirchhoff Prestack Depth Migration

In 1954, Hagedoorn developed the first version of diffraction stack migration by manually constructing diffraction curves (*curves of maximum convexity*). His considerations provide the basis for modern Kirchhoff Prestack Depth Migration schemes assuming that reflectors are build up of closely spaced diffraction points.

A single diffraction point P_D in the subsurface acts as a Huygen's secondary source which maps onto a diffraction hyperbola in the time section if it is placed in a constant velocity medium. This hyperbola, generally called diffraction curve (2D) or diffraction surface (3D) in inhomogeneous media, collects all data samples with the respective travel time from source to diffractor and back to the i^{th} receiver ($t_S + t_{R_i}$, $i = 1, \ldots, n$). The summation of all amplitudes along the diffraction curve yields a value which is then assigned to the respective subsurface point. At last, this leads to an image of the diffraction point itself at the correct position within

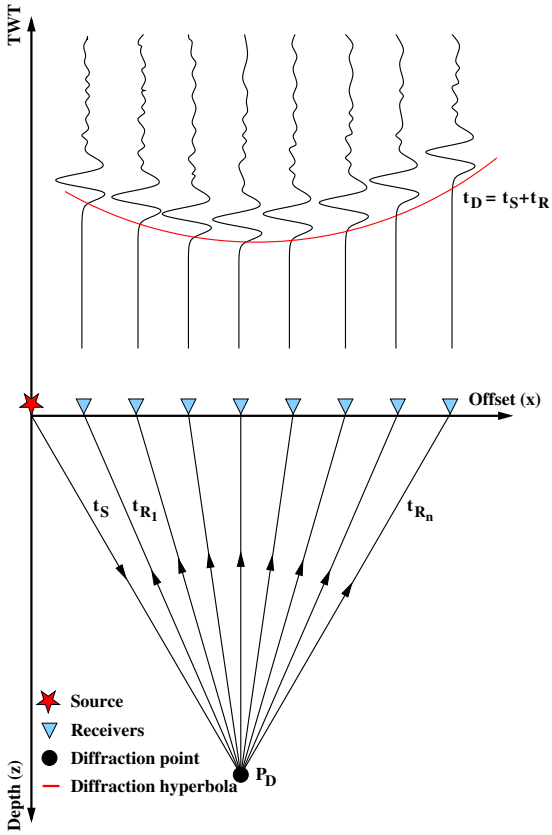

Figure 4.1: A single diffractor located in a medium with constant velocity illustrates the principle of diffraction stack.

the resulting depth section. Figure 4.1 demonstrates this procedure. Here, the diffraction curve is illustrated as a red line in the shot gather. The latter results from a single shot (red star) where the signals were recorded by several equally spaced receivers (blue triangles). The black circle marks the diffraction point P_D.

For a reflector, consisting of closely spaced diffraction points (Figure 4.2 (a)), the diffraction curves superimpose and diffractions within the time section are only visible at both ends of the reflection event (Figure 4.2 (b)). This illustration indicates how the method works in principle. Firstly, diffraction curves for any given subsurface point (usually predefined as a dense grid) have to be calculated. Then, the amplitudes have to be summed along these curves. Thereby, the summation of coherent signals results in high values (constructive interference), whereas the sum of noise is very small (destructive interference). At last, the results have to be placed to the corresponding depth points within the grid.

An enhancement of the above method is provided by the Kirchhoff Prestack Depth

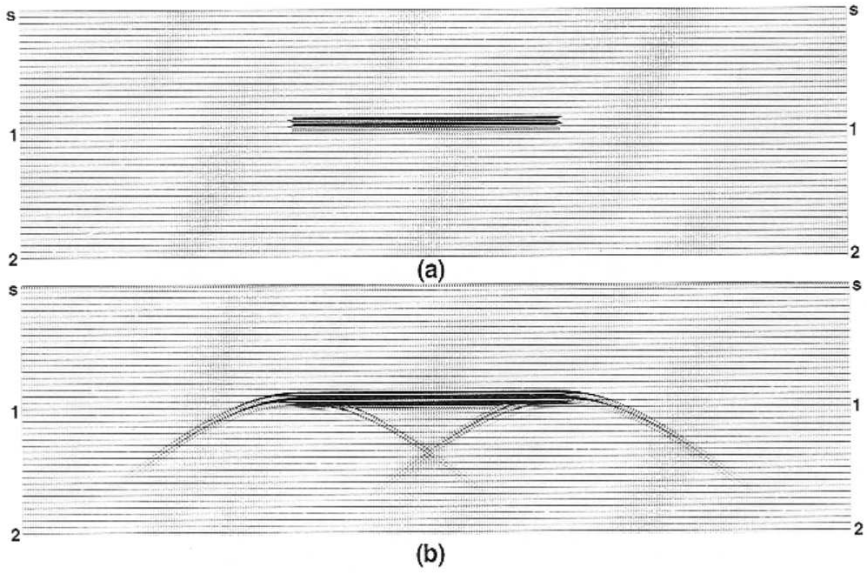

Figure 4.2: If the diffraction points are spaced closely enough, the corresponding diffraction curves superimpose and diffractions are only evident at both ends of the reflection (from Yilmaz, 2001).

Migration method which is in principle a weighted diffraction stack. It is based on the Kirchhoff integral solution (Schneider, 1978) of the wave equation

$$\nabla^2 u = \frac{1}{v^2}\frac{\partial^2 u}{\partial t^2}\,. \tag{4.1}$$

where u is the wavefield and v denotes the wave velocity. Equation 4.1 represents a scalar form of the wave equation. The solution of equation (4.1) in form of the Kirchhoff integral describes the wavefield at any subsurface point within the medium. This can be done by spatial integration of the weighted time derivatives of the wavefield at the point of observation (usually the geophone location at the surface). The migrated section $V(\vec{m})$ at any subsurface point $\vec{m}(x, y, z)$ can then be formulated in the most general case as a surface integral over the aperture A (e.g. Schleicher *et al.*, 1993)

$$V(\vec{m}) = \frac{-1}{2\pi}\iint\limits_A w(\vec{m},\vec{x})\,\dot{u}(\vec{x}, t_S + t_R)\,d\vec{x}\,. \tag{4.2}$$

The weight function $w(\vec{m},\vec{x})$ in equation (4.2) is used to account for the correct treatment of amplitudes during the back propagation of the wavefield (Goertz, 2002), i.e. it involves the adjustment of the amplitudes for obliquity and geometrical spreading. In order to correctly recover the source pulse, the time derivative of the input wavefield $\dot{u}(\vec{x}, t_S + t_R)$ is needed (Newman, 1975) where $t_S(\vec{x_S},\vec{m})$ and $t_R(\vec{m},\vec{x_R})$ are the

travel times from the source at position $\vec{x}_S$ to the image point in the subsurface and from the latter to the receiver at $\vec{x}_R$, respectively. The step by step evolution from Hagedoorn's principle to modern Kirchhoff methods is well explained in Bleistein (1999) and Bleistein & Gray (2001).

4.2 Travel time estimation

Kirchhoff Prestack Depth Migration requires travel time information since it is implemented as a weighted stack of the time derivatives of the recorded wavefield along diffraction curves. For this purpose, a method has to be chosen which provides both, an accurate solution valid for the frequency content of the recorded seismic signals and a robust travel time determination taking into account the complexity of the velocity model. Most of the proposed techniques are based on the solution of the eikonal equation which describes wave propagation in a high frequency approximation of the scalar wave equation (e.g. Červený & Hron, 1980). Two different velocity models for each area of interest were used in this work: the first one is generated by westward extending a reliable model for the forearc region at 23.25°S and the second one is obtained using the velocity information from wide-angle investigations. In this section these velocity models are presented and discussed and a brief introduction of the travel time calculation procedure is given.

4.2.1 Modelling of the velocity fields

A reliable velocity model was provided for the eastern part of line SO104-13 including the trench region as well as the subsurface below the lower and middle continental slope (Caesar R. Ranero, IFM-Geomar, Kiel, pers. comm.). This model of the velocity structure in the trench and forearc region enabled to build extended models for both areas of interest. This is done by assuming that the overall velocity structure does not change significantly from south to north. This assumption is also supported by the observations from wide-angle measurements presented in Patzwahl (1998).

The exact depth of the ocean bottom seaward of the trench was determined by migrating the data with a constant water velocity of approximately 1500 m/s. Then, the ocean bottom was picked manually within the obtained depth images. At last, the subsurface velocities were determined by extending the existent velocity information using the same gradient. The resultant models (denoted *IFM-model* in the following) for line SO104-07 and line SO104-13 are illustrated in Figures 4.3(a) and (b), respectively. The maximum velocity (about 7500-8000 m/s) is found below the

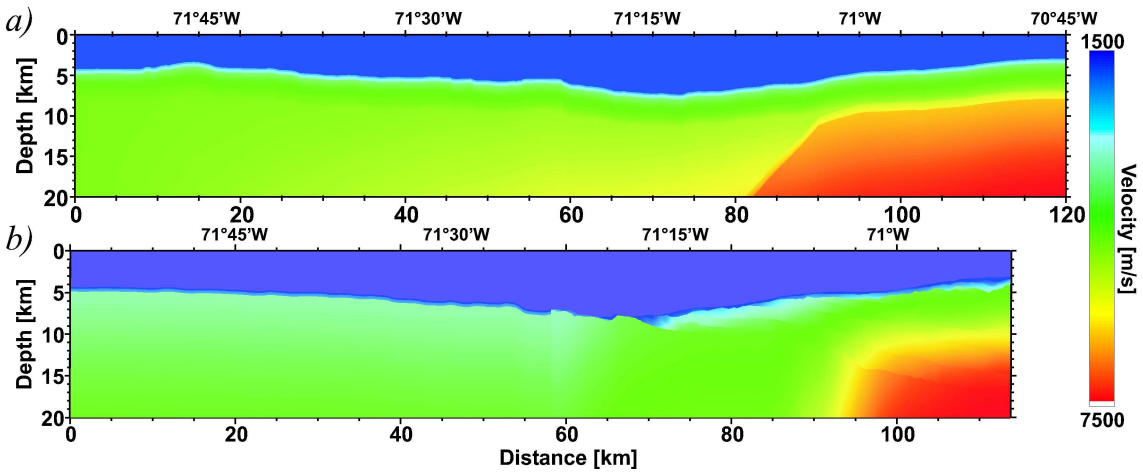

Figure 4.3: 2D velocity models used for Kirchhoff Prestack Depth Migration, where (a) is the model for line SO104-07 and (b) for line SO104-13, respectively. The eastern part of the lower model (line SO104-13) which included the trench and the forearc region was kindly provided by Cesar Ranero (Geomar, Kiel).

continental slope at depths ranging from 10 km to 20 km. Unfortunately, the velocities estimated for these models are not fully consistent with observations from wide-angle seismics.

To overcome this problem, the western part of the above models was revised. Thereby, the boundary velocities determined from wide-angle measurements were taken into account (see Patzwahl *et al.*, 1999 and references therein). A cross section obtained from wide-angle seismics along 23.25°S is illustrated in Figure 4.4. Here, the seismic boundaries are shown as solid black lines. Between these seismic boundaries a constant velocity gradient was assumed. Another problem arose since the resulting velocity field did not match the IFM-model near the trench. Combining the new velocity field with the IFM-model was only possible if much higher velocities are presumed in depth ranges between 10 km and 20 km than proposed within the IFM-model. Nevertheless, this presumption coincides with the wide-angle results (cf. Figure 4.4).

The construction of the new velocity field (denoted *wide-angle model* in the following) was accomplished by assuming the Moho depth at about 7 km underneath the upper boundary of the Nazca plate. Since the ocean bottom shows topography the interface between oceanic crust and mantle has to be smoothed to avoid a mapping of this roughness to the Moho within the model. This is done by using the quadratic regression function

$$z_{smooth}(x) = p_1 x^2 + p_2 x + p_3 \,, \tag{4.3}$$

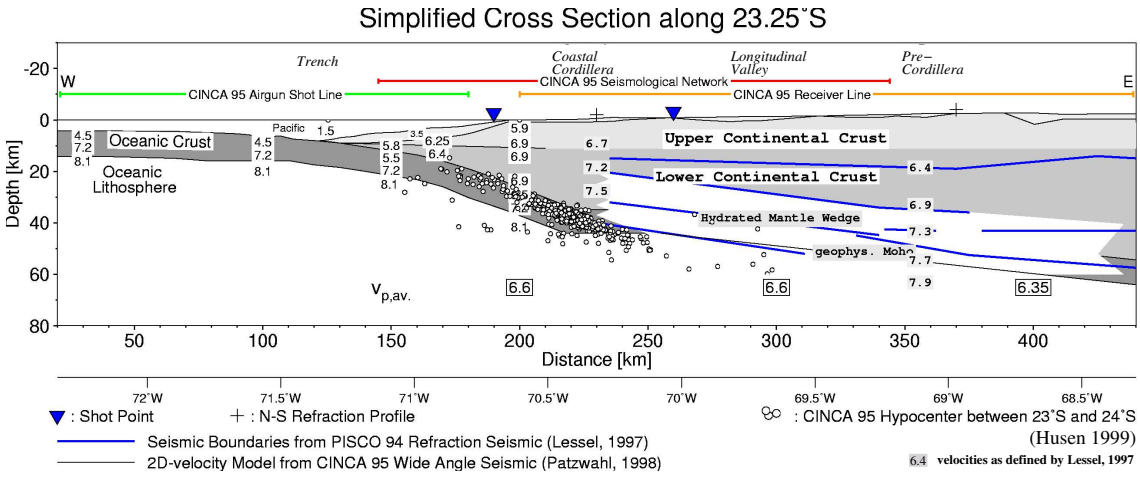

Figure 4.4: Results from wide-angle seismics for line SO104-13 (Patzwahl, 1998) including seismic boundaries estimated from refraction seismic data acquired during the PISCO experiment (Lessel, 1998) and the hypocenters of the Antofagasta aftershock series recorded by the CINCA network (Husen, 1999).

where p_1, p_2 and p_3 are the respective fitting parameters, x denote the horizontal distance from the origin of the model and z_{smooth} is the new Moho depth. Due to the different curvature of the upper plate boundary west and east of the trench this procedure had to be done separately for both parts. To complete the models, the P-wave velocities of the overriding continental crust were taken from the IFM-models and included into the wide-angle models. In contrast to the IFM-models, the maximum velocities of the resultant fields (Figure 4.5) appear below the oceanic Moho with values of approximately 8500 m/s to the west of the trench.

The accuracy of the wide-angle model strongly depends on the localisation of the seismic boundaries. Furthermore, the velocity information between these boundaries in Figure 4.4 is an averaged value which additionally complicates the construction of a reliable model. A discussion whether the IFM-model is more accurate than the wide-angle model or vice versa is given by means of some depth images in chapter 5 on page 61.

4.2.2 Travel time calculation

Audebert *et al.* (2001) made a coarse classification of the various travel time estimation techniques. They differentiate between limited bandwidth methods, i.e. methods working with frequency dependent Green's functions, and infinite frequency methods. The latter comprise the classical ray based computation algorithms, which are in particular the paraxial and dynamic ray tracing (Červený & Hron, 1980;

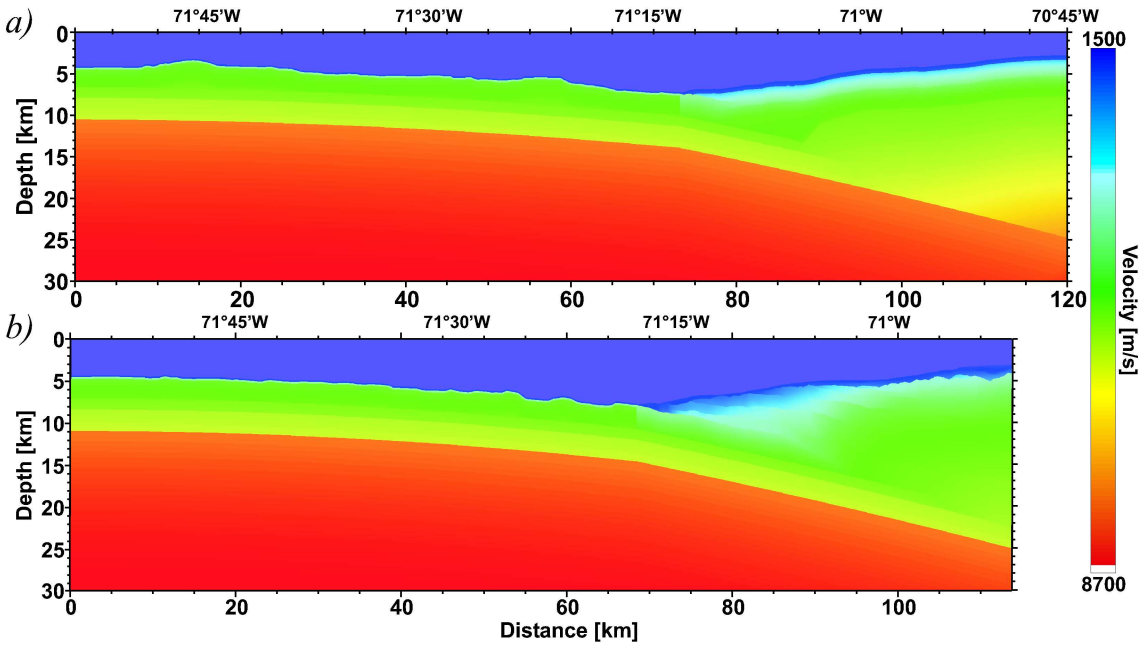

Figure 4.5: Modified velocity models for (a) line SO104-07 and (b) line SO104-13 taking wide-angle results into account. The Moho depth is assumed to be located at about 7 km below the seafloor. Continental crust velocities are the same as in the models shown in Figure 4.3.

Beydoun & Keho, 1987), but also the modern finite difference (FD) solutions to the eikonal equation (Vidale, 1988; Van Trier & Symes, 1991; Podvin & Lecomte, 1991). The main advantages of the FD schemes over ray tracing are the fast and robust computation of the travel times. This is caused by the fact that during ray tracing a large number of rays have to be computed for each subsurface point but, at last, only one has to be picked that leads to the desired first arrival time. Also the appearance of shadow zones, where no ray reaches the considered region at depth, and the approaches to circumvent this problem immensely increase the computational cost for standard ray tracing techniques.

In contrast, finite difference travel time estimation techniques propagate wave fronts rather then rays in the velocity (or slowness) model (so-called *expanding wavefront methods*; Audebert *et al.*, 2001 q.v.). In this thesis a FD algorithm proposed by Podvin & Lecomte (1991) was used to calculate the required travel times. It is a kind of improvement of a finite difference approach firstly presented by Vidale (1988). Thereby, local travel times are computed at each grid-point by applying successively Huygen's principle in combination with a linear interpolation to calculate incremental travel times for grid points which are not actually timed. This linear interpolation is similar to a local plane wave approximation. The first ar-

rivals are then obtained using a minimum-time criterion (Fermat's principle). The accuracy of this method mainly depends on the grid spacing of the velocity model. Three propagation modes can be handled by this algorithm, i.e. diffractions, head waves as well as plane waves. A comprehensive overview of some travel time computation methods and a detailed discussion of the advantages and disadvantages of these methods can be found in Leidenfrost *et al.* (1999) and Audebert *et al.* (2001).

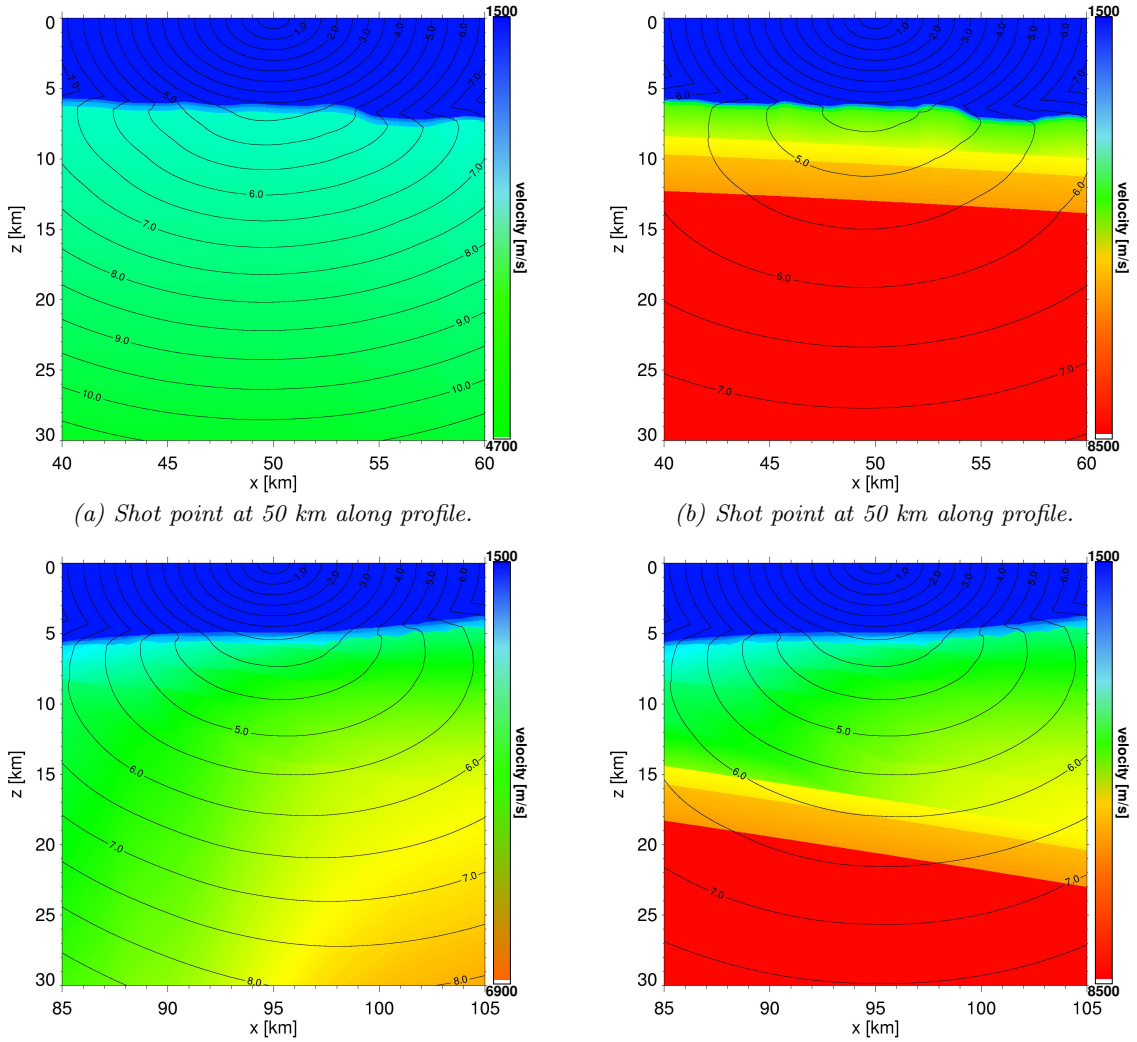

(a) Shot point at 50 km along profile.

(b) Shot point at 50 km along profile.

(c) Shot point at 95 km along profile.

(d) Shot point at 95 km along profile.

Figure 4.6: Isochrons plotted over the corresponding part of the velocity model. (a) Travel times estimated for a shot point located 50 km along profile with the help of the IFM-model. (b) Same as (a) but calculated with the wide-angle model. (c) and (d) Travel times underneath the continental slope at 95 km calculated with the IFM-model and the wide-angle model, respectively.

Some examples for the resulting travel times from line SO104-13 are presented in Figure 4.6. The isochrons were plotted over the corresponding part of the velocity field. On the left hand side (Figures 4.6(a) and (c)), the results of travel time calculation with the IFM-model are illustrated whereas on the right hand side the respective travel times from the wide-angle models are shown. To the west of the trench, at 50 km along profile, the maximum travel time reaches about 10.5 s at the lower boundary of the IFM-model (Figures 4.6(a)) but only 8 s in the wide-angle model (Figures 4.6(b)). To the east of the trench (Figures 4.6(c) and (d)) this difference decreases due to the fact that the velocities in the overriding plate are similar within both models.

4.3 Influence of the velocity field on travel time estimation

The velocity distribution in the subsurface significantly influences the travel time calculation and thus the migration results. Higher velocities generally image reflection events at greater depths. Figure 4.7 illustrates the differences between the respective models by means of two velocity-depth functions. The blue curves correspond to velocities west of the trench at about 30 km along profile for line SO104-07 (Figure 4.7(a)) and respectively 25 km for line SO104-13 (Figure 4.7(b)). Directly

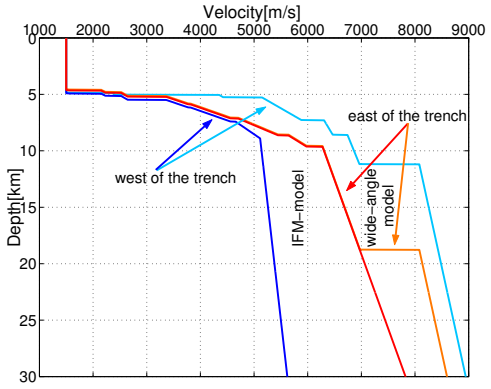

(a) Velocity-depth plot of the models for line SO104-07.

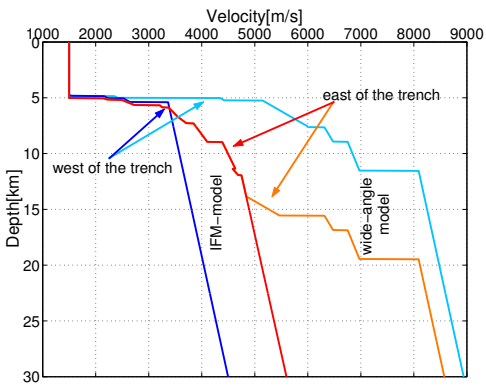

(b) Velocity-depth plot of the models for line SO104-13.

Figure 4.7: Comparison of the used velocity models by means of two representative depth functions from east (red and orange) and west of the trench (blue and cyan) for both profiles, respectively. The velocities in the subsurface to the west of the trench show significant differences between the models. Further to the east underneath the continental slope (red and orange lines) the IFM-model and the wide-angle model are quite similar down to a depth of approximately 15 km. Below this depth, the difference between the curves increases.

below the ocean bottom between 5 km and 6 km, the IFM-models (blue curves) exhibit a gradient from about 2000 m/s to 3500 m/s whereas the wide-angle models (cyan curves) show near surface velocities of 4500 m/s as proposed by the wide-angle investigations. Those values between 4000 m/s and 4500 m/s are typical for the upper part of the oceanic crust but the actual location of the transition zone from lower velocities to the above values is not well constrained.

In deeper regions especially for line SO104-13, the IFM-models contain a relatively smooth gradient reaching maximum velocities of 4500 m/s and 5500 m/s, respectively. Probably, these maxima are too low compared to the expected velocities at depth ranges below the oceanic Moho. In contrast, velocities were obtained up to 8000 m/s at about 7 km below the seafloor in the wide-angle models which are with respect to the wide-angle results and from global observations closer to reality. The values within the upper and lower continental crust are similar for both models (red and orange curves). At that depth range where the slab is suggested, the difference between both velocity curves increases to about 3000 m/s for line SO104-13 (at 90 km along profile; Figure 4.7(b)) but only to less than 1000 m/s for line SO104-07 (at 95 km; Figure 4.7(a)). However, the difference in the south (line SO104-13) decreases further to the east due to a lateral velocity gradient (cf. Figure 4.3) so that the resulting images of this area are similar for both models (see chapter 5).

4.4 Principles of Fresnel Volume Migration

The Fresnel Volume Migration, as used for the investigations presented here, can be seen as an extension of Kirchhoff Prestack Depth Migration (e.g. Goertz *et al.*, 2003; Lüth *et al.*, 2005). The basic idea of this scheme is to restrict the migration operator in a form that the resulting image of a recorded event is limited to the volume in the subsurface that physically contributes to the reflected signal (Lüth *et al.*, 2005). This is, in fact, the first Fresnel volume (e.g. Kravtsov & Orlov, 1990; Kravtsov, 2005). To realize this limitation in practice, an additional weight function is included into the diffraction stack integral (equation (4.2)). Since the used Fresnel volume calculation is based on a ray tracing formalism, the knowledge of the emergence angles of the waves arriving at the receivers is essential. This angle information is needed as the starting direction for ray tracing.

4.4.1 Fresnel zones

The concept of the Fresnel zones originally stems from physical optics. In geophysics, two slightly different definitions of the Fresnel zones size can be found (see Figure

4.8). The most common one, presented by Sheriff (1980), characterizes it as that part of a reflector in the subsurface from which the reflected energy can reach a receiver within half the wavelength λ of the first reflected energy. He describes the outer border of the first Fresnel zone as those points on the reflector where constructive interference is completely disabled (magenta seismogram in Figure 4.8). Berkhout (1984) defines the Fresnel zone as the zone from where the arriving energy

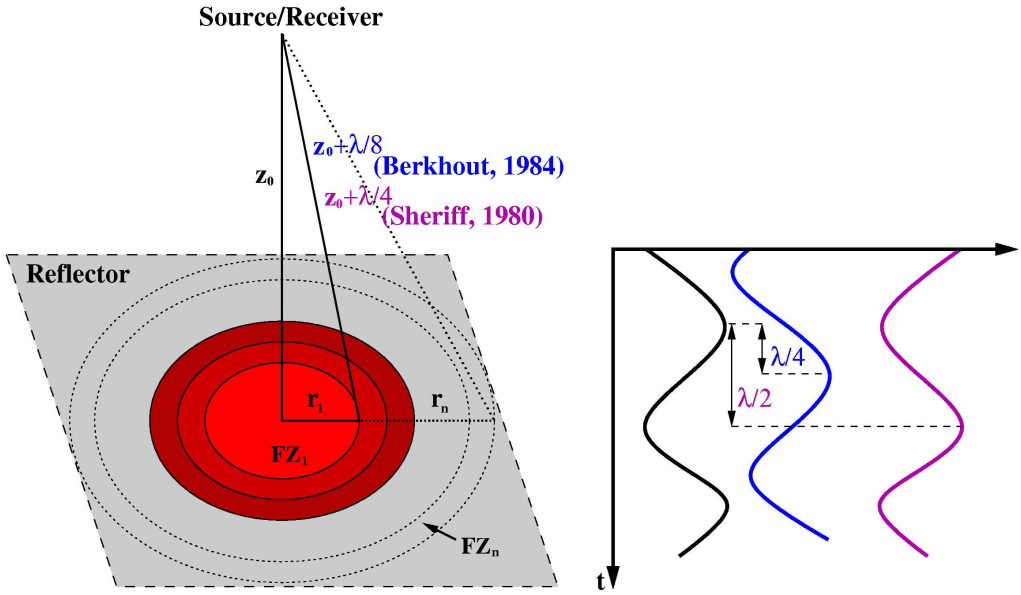

Figure 4.8: Left: Illustration of Fresnel zones of n^{th} order on a horizontal reflector. Source and receiver are situated at the same location (zero offset configuration). Around the center, the first Fresnel zone (light red area) is circular whereas the outer Fresnel zones are annular rings (dark red areas). Right: Simplified sketch of a reflection from the midpoint of the first Fresnel Zone (black seismogram) and from the edge of it. The blue seismogram corresponds to the Berkhout criterion and the magenta one to Sheriffs definition.

has a maximum difference of the phases not larger than one-quarter wavelength. This criterion corresponds to the transition points from constructive to destructive interference (blue seismogram in Figure 4.8). However, both definitions can be used to study the resolution of a horizontal reflector (e.g. Hagedoorn, 1954; Sheriff, 1977; Eaton *et al.*, 1991) or, as it will be presented in the following, to improve seismic images.

For a zero offset configuration, the Fresnel zones on a horizontal reflector are centered perpendicular beneath the source/receiver location (Figure 4.8). Thereby, the first Fresnel zone is circular, whereas Fresnel zones of higher order are annular rings with successively larger radii. In this zero offset case, the radius of the first Fresnel zone for

point sources can be estimated using the Pythagorean theorem $r_1^2 = \lambda z_0/2 + \lambda^2/16$ (Sheriff) or $r_1^2 = \lambda z_0/4 + \lambda^2/64$ (Berkhout). If the λ^2 term is small, it can be neglected and the radius can be written as (e.g. Sheriff, 1980; Eaton *et al.*, 1991)

$$r_1 \approx \sqrt{\frac{\lambda z_0}{2}} = \frac{V}{2}\sqrt{\frac{t}{\nu}} \quad \text{Sheriff}\,, \tag{4.4}$$

$$r_1 \approx \sqrt{\frac{\lambda z_0}{4}} = \frac{V}{2}\sqrt{\frac{t}{2\nu}} \quad \text{Berkhout}\,, \tag{4.5}$$

for an interface depth of z_0, where λ and ν are the wavelength and the frequency, respectively. Thereby, the reflector depth z_0 can be expressed in terms of the velocity V and the two-way-travel time t using the relationship $z_0 = Vt/2$. The wavelength and the frequency are connected via $\lambda = V/\nu$.

4.4.2 Fresnel volume determination

Besides the frequency dependence of the radii (equation (4.5)), in a real experiment the size of a Fresnel zone is also controlled by the source and receiver locations of the seismic array. The most general formulae to evaluate Fresnel zones in complex media are firstly determined by Gelchinsky (1985). More useful for the given problem is the concept of Fresnel volume ray tracing as proposed by Červený & Soares (1992). Based on the paraxial ray theory (Beydoun & Keho, 1987; Červený, 2001), the first Fresnel zones are calculated for each point of a ray within a standard ray tracing scheme. Červený & Soares (1992) used a travel time formulation (equation (4.6)) which redefines the Fresnel volume definition given by Kravtsov & Orlov (1990). It defines a criterion if an arbitrary point P in the vicinity of a ray connecting the source point S and the receiver R belongs to the corresponding Fresnel volume. This is the case if

$$|t(S,P) + t(P,R) - t(S,R)| \leq \frac{1}{2}T\,, \tag{4.6}$$

where $t(S,P)$ and $t(P,R)$ are the travel times from the source to point P and from the latter to the receiver, respectively. The travel time of the direct wave from the source to the receiver is $t(S,R)$ and T denotes the dominant period. For a constant velocity model equation (4.6) can be rewritten as

$$|s + r - l| \leq \frac{1}{2}\lambda\,. \tag{4.7}$$

Here, l is the length of the ray from source S to receiver R via the reflection point M, and s and r are the ray lengths from source via point P to the receiver, respectively (see Figure 4.9). For a reflection at point M, equation (4.7) states that an arbitrary

point P on the corresponding isochron (line of constant two-way-travel time) is located inside the first Fresnel zone of the ray $\overline{SMR}$, if the difference between the length of the latter and the length of the ray $\overline{SPR}$ is less (or equal) than half the wavelength λ. As reflection seismics usually works with band-limited waves, the dominant wavelength should be used within this formula.

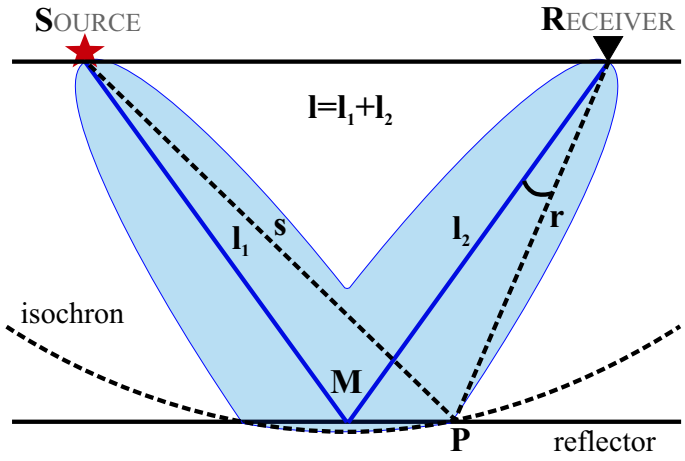

Figure 4.9: Fresnel volume (blue area) of a reflected ray in a constant velocity medium. It starts at the source point S, reaches the reflection point M and ends at the receiver R. The ray length from the source point to the receiver via M is l (blue line) and it is $r+s$ for a ray path via an arbitrary point P (dashed black line) located on the corresponding isochron (curved dashed line). The difference between the measured and the expected polarization is specified by the angle γ.

4.4.3 Fresnel weight

To make the Fresnel volume definition applicable within a standard migration procedure, the criterion (equation (4.7)) has to be modified with respect to the emergence angle at the receiver. Figure 4.9 shows the part of a Fresnel volume (blue area) on the isochron that belongs to a reflection in a homogeneous medium at the reflection point M. The difference between the measured propagation direction of a P-wave from reflection point M and the expected direction from point P at the geophone is expressed in terms of the angle γ. Goertz *et al.* (2003) derived that any arbitrary point P on the isochron is located within the n^{th} Fresnel volume if

$$\cos\gamma \geq \frac{2r^2+2rs-n(r+s)\lambda+n^2\frac{\lambda^2}{4}}{2r^2+2rs-nr\lambda} = H_n \quad [n=1,2,\dots]\,. \tag{4.8}$$

This formulation of a Fresnel criterion for homogeneous media enables to find a weight function W_F which can be inserted into the diffraction stack integral (equa-

tion (4.2)) and which depends on the size of the Fresnel zone on the isochron. Lüth *et al.* (2005) proposed a function that benefits summation within the first Fresnel zone and that avoid summation for Fresnel zones of order higher than two by setting the weighting factor to zero (equation (4.9)). To suppress migration artifacts due to the limited aperture, they included the second Fresnel zone where W_F is linearly tapered with increasing angle γ:

$$W_F = \begin{cases} 1 & : \quad \cos\gamma \geq H_1\,, \\ \frac{\cos\gamma - H_2}{|H_1 - H_2|} & : \quad H_1 > \cos\gamma \geq H_2\,, \\ 0 & : \quad \cos\gamma < H_2\,. \end{cases} \tag{4.9}$$

Here, H_1 and H_2 are the right hand side terms of equation (4.8) for $n = 1$ and $n = 2$, respectively. Inserting this definition of a weight function into equation (4.2), the diffraction stack integral reads

$$V(\vec{m}) = \frac{-1}{2\pi} \iint\limits_A W_F w(\vec{m}, \vec{x})\, \dot{u}(\vec{x}, t_S + t_R)\, d\vec{x}. \tag{4.10}$$

Again, $V(\vec{m})$ is the migrated image at the image point $\vec{m}(x, y, z)$ in the subsurface but now constructed as a restricted summation along the isochrons. The term $w(\vec{m}, \vec{x})$ is the true-amplitude weight function and $\dot{u}(\vec{x}, t_S + t_R)$ represents the derivative of the input wavefield whereas $t_S(\vec{x_S}, \vec{m}) + t_R(\vec{m}, \vec{x_R})$ are the travel times from the source location $\vec{x_S}$ to the image point and respectively from the latter to the receiver $\vec{x_R}$.

4.4.4 Fresnel volume ray tracing in heterogeneous media

In contrast to the above described homogeneous case, the rays in heterogeneous media are no straight lines but they might be curved in a complex way which makes the computation of the Fresnel volumes much more difficult. Travel time fields from source and receiver can be used (Kvasnička & Červený, 1994) but if the travel times from the reflector are not known the use of this approach is not helpful. Another possibility is to calculate the paraxial Fresnel volumes as proposed by Červený & Soares (1992) directly from the rays. In general, the location of a reflector at depth is unknown and thus a ray tracing method was used which traces the direct ray from the receiver to the corresponding virtual source point S' in the subsurface but not the reflected ray, i.e. that ray from the receiver via point M to the source as illustrated in Figure 4.10. The resulting direct Fresnel volume (red area in Figure 4.10) is used as an approximation of the Fresnel zone on the reflector. Thereby,

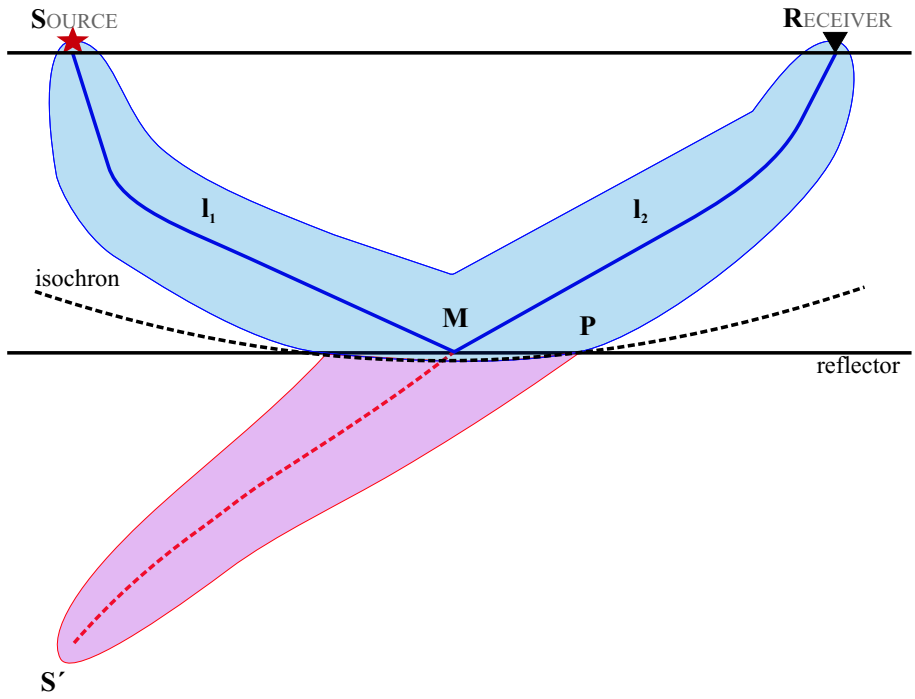

Figure 4.10: Fresnel volume of two rays in a heterogeneous medium. The reflected ray from the source to the receiver is colored blue with the corresponding Fresnel volume (light blue area). A ray tracing scheme was used which produces the direct ray from R to S' (dashed red line) since in general the location of the reflector is not known. The corresponding Fresnel volume is illustrated by the light red area.

an error can occur if the velocity below a possible reflector increases (or decreases). The case of increasing velocity with depth is discussed in detail in section 4.6.

Lüth *et al.* (2005) followed the strategy of Červený & Soares (1992) and used the paraxial Fresnel volume estimation. They simplified the formulation by Červený & Soares under the assumption that velocity models used for seismic imaging are in general smooth. They derived a formulation for an approximate Fresnel volume with a circular shape where the radius of the Fresnel zone is perpendicular to the ray. Thus, the Fresnel radius r_Q of any point Q of the ray can be described in the form

$$r_Q \approx \sqrt{\frac{T}{\frac{1}{\Pi_{13}(Q)} - \frac{1}{\Pi_{13}(Q)\,\Pi_{13}(S')}}}\,. \tag{4.11}$$

In equation (4.11) the terms $\Pi_{13}(Q)$ and $\Pi_{13}(S')$ give the expressions for the ray propagator elements at ray point Q and at the virtual source point S', respectively. A detailed description of the ray propagator matrix can be found in Červený (2001). Here, the estimated radii belong to the first Fresnel volume of the ray. Thus, the

weight function (equation (4.9)) can be modified for heterogeneous media as

$$W_F(r_I, r_Q) = \begin{cases} 1 & : \quad r_I \leq r_Q \,, \\ 1 - \frac{r_I - r_Q}{r_Q} & : \quad r_Q < r_I \leq 2r_Q \,, \\ 0 & : \quad r_I > 2r_Q \,, \end{cases} \tag{4.12}$$

where r_Q is the radius of the first Fresnel volume at ray point Q and r_I is the distance of the considered image point from the ray. In equation (4.12) the radius of the second Fresnel volume is approximated by $2r_Q$.

4.5 Estimation of the emergence angle

One of the most important preconditions for Fresnel Volume Migration is a reliable knowledge of the emergence angle used as the initial input for ray tracing. For three-component data the polarization information can be used (Lüth *et al.*, 2005) but the CINCA profiles are 2D single component (marine) data sets so that other methods had to be considered to obtain the emergence angles at the surface for each sample within the shot gathers. An adequate procedure is the calculation of the apparent velocity (horizontal slowness) of the wavefront along the acquisition surface.

So far, several techniques have been developed to extract slowness information from seismic data, most of them based on plane-wave decomposition of seismograms (e.g. Müller, 1971; Treitel *et al.*, 1982). Based on the Radon transform (Radon, 1917, section 3.2), the best-known technique to estimate the horizontal slowness might be the slant stack method, where the data are transformed from the time-distance ($t-x$) to the intercept time-ray parameter ($\tau - p$) domain (e.g. McMechan & Ottolini, 1980; Chapman, 1981). Summing up the samples along lines of constant $\Delta t/\Delta x$ (or similarly p), all crossing the sample of the center trace with the intercept time τ within a predefined window, the instantaneous slowness $p_x(x,t)$ can be derived by weighting the slant stacks by coherence (e.g. McMechan, 1983; Milkereit, 1987b). A disadvantage of this method is that the slant stack does not preserve phase and amplitude information when the source is a point source (e.g. Wang & Houseman, 1997). To avoid problems with surface data excited by a point source a cylindrical $\tau - p$ transform is required (e.g. Harding, 1985; Fokkema *et al.*, 1992).

Other techniques, working with coherence measurements of waveforms over finite distance-time windows, are the beamforming method, discussed e.g. by Dudgeon & Mersereau (1984), semblance analysis (e.g. Neidell & Taner, 1971; Stoffa *et al.*, 1981) and the multichannel cross-correlation method (Haslinger, 1994). Heigel (2005) compared the latter with the slant stack and the semblance analysis and concluded that

the cross-correlation leads to the most stable results. In this work, his implementation was used to calculate the necessary horizontal (and vertical) slowness for the CINCA data sets.

4.5.1 Slowness extraction from real data

In contrast to other techniques, the multichannel cross-correlation works with two time windows of the same size. Thereby, one of them, called *reference window*, is centered on a data sample $S(x,t)$ at time t of a trace with offset x from the source. The maxima of the cross-correlation between the samples in the reference window and each segment of n adjacent traces, defined by the second time window, yield the time shifts associated with the most coherent signals within the windows (Tillmanns & Gebrande, 1999 q.v.). Plotting these time shifts against the distance from the reference trace and calculating the slope of the best fit after a linear regression directly leads to the local horizontal slowness because of the relation $p_x(x,t) = \frac{\Delta t}{\Delta x}$. The z-component of the slowness vector (vertical slowness) is then related to p_x via $p_z(x,t) = \sqrt{\frac{1}{v_0^2} - p_x^2(x,t)}$, where v_0 is the near surface velocity. In 2D, this usually results in two additional input sections for Fresnel Volume Migration which have the same size as the shot gather: a horizontal and a vertical slowness gather (see Figure 4.11). The number of traces n used within this procedure has to be chosen with respect to the spatial extent of linear signal coherence in the data (Haslinger, 1994; Tillmanns & Gebrande, 1999). A detailed description of the used technique and a solution of the problems appearing at the edges of the shot gathers and zero traces can be found in Heigel (2005).

The temporal and spatial extension of the used windows were estimated using the dominant period $1/f_{dom}$ and, respectively, the dominant wavelength λ_{dom}. Therewith, the number of traces n and the number of time samples m can be defined by

$$\begin{aligned} n &\approx \frac{\lambda_{dom}}{dx} \\ m &\approx \frac{1}{f_{dom} dt}, \end{aligned} \tag{4.13}$$

where dt is the sample rate of the data and dx is the geophone spacing. As seen in equation (4.13), an increase of the dominant frequency results in a shorter time window and in a decrease of n. However, Heigel (2005) proposed that the number of traces on both sides of the reference trace should be at least $n = 4$ to suppress possible errors during slowness computation.

4.6 Implementation of Fresnel Volume Migration

Figure 4.11 describes the principal workflow of the Fresnel Volume Migration procedure. The blue boxes illustrate the necessary preprocessing steps such as filtering and travel time calculation. Compared to Kirchhoff Prestack Depth Migration an additional external slowness calculation has to be carried out which yields the required angle information as an initial parameter for the ray tracing procedure. The main Fresnel Volume Migration routine (red box) requires a couple of additional input parameters (green box) which are usually not needed for Kirchhoff Prestack Depth Migration. The main processing includes ray tracing and the calculation of the Fresnel radii as well as the estimation of the weighting factor. The last step comprises the weighted summation of the amplitudes.

In this section, at first some of the results from the slowness calculation are presented

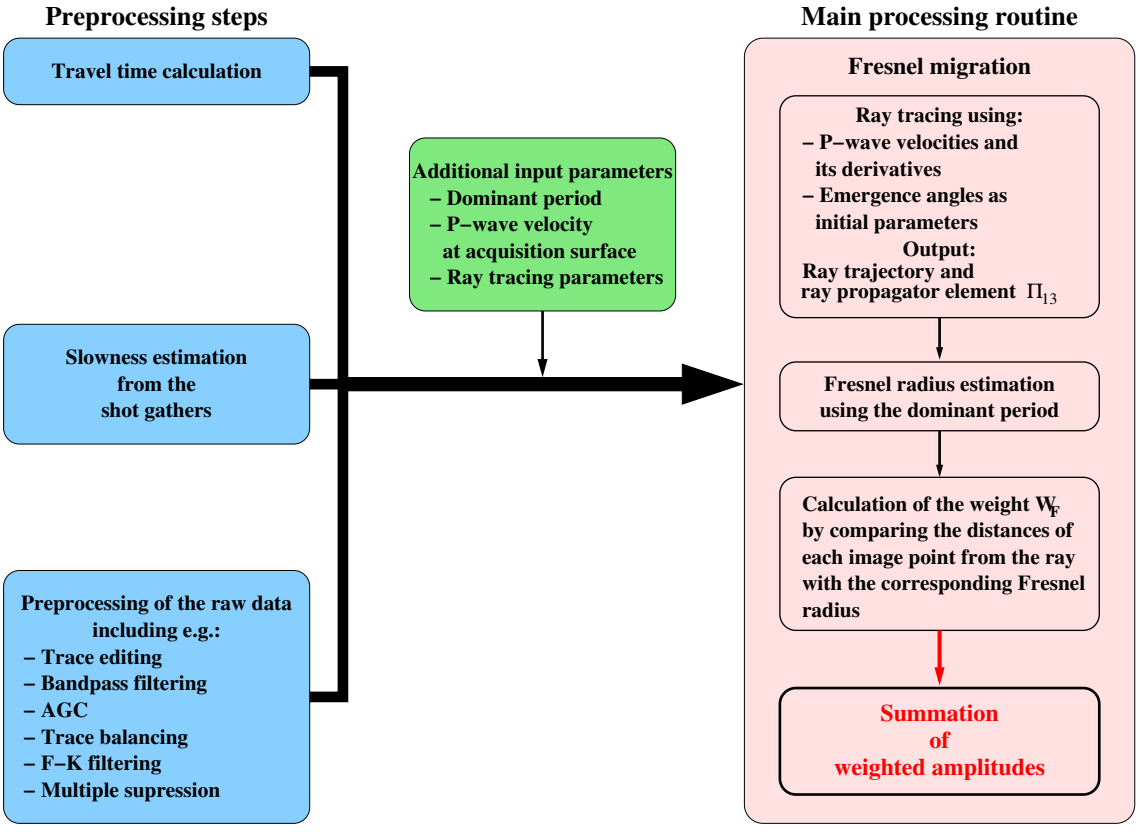

Figure 4.11: Workflow of the Fresnel Volume Migration. The colored blue boxes indicate the pre-information needed. The main Fresnel Volume Migration routine needs several input parameters stated in the green box. Within the red box, the particular subroutines of the Fresnel Volume Migration are depicted.

and discussed prior to the description of the ray tracing procedure and the resulting Fresnel weight.

4.6.1 Slowness calculation for the CINCA data sets

Both, the slowness estimation algorithm by Heigel (2005) (equation (4.13)) and the Fresnel routine require information about the dominant frequency (equation (4.11)). Figure 4.12 illustrates the power spectra for two representative shot gathers of line SO104-07 and line SO104-13, respectively. While the spectrum of line (SO104-13) shows a clear dominant frequency around 30 Hz (Figure 4.12(b)), several peaks were found in the spectrum of the shot gather from line SO104-07 (Figure 4.12(a)). For both profiles, the slowness was calculated with a dominant frequency of $f_{dom} \approx 27$ Hz (in water λ_{dom} equals approximately 55 m) and 4 neighbouring traces for cross-correlation with the respective reference trace. To test the influence of the dominant frequency, the slowness was additionally calculated with $f_{dom} = 42$ Hz for line SO104-07 which results in approximately half the temporal window size. The comparison of the horizontal slowness results for a shot gather of line SO104-07 is illustrated in Figure 4.14.

The slowness sections from line SO104-07 (Figure 4.14) reflect the most prominent

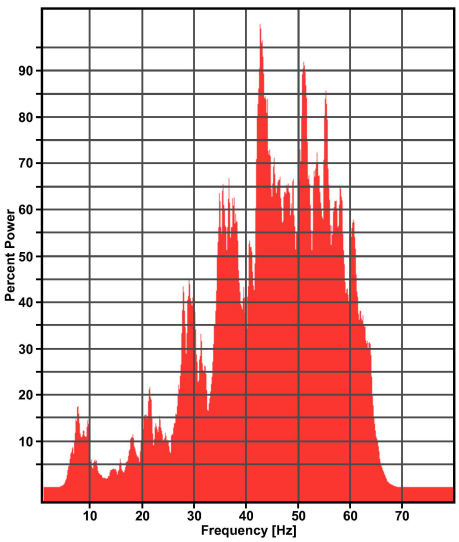

(a) Power spectrum of shot 510 line SO104-07.

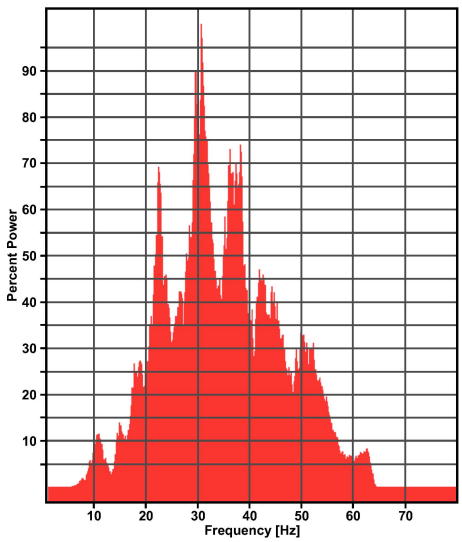

(b) Power spectrum of shot 10 line SO104-13.

Figure 4.12: Power spectra of two representative shots from (a) line SO104-07 and (b) line SO104-13. The spectrum in Figure 4.12(b) exhibits an explicit peak at about 30 Hz while that of the shot gather from line SO104-07 shows three different maxima at approximately 42 Hz, 51 Hz and 55 Hz.

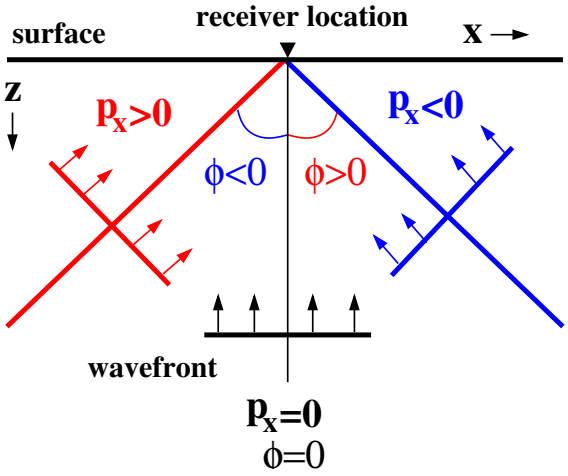

Figure 4.13: Sketch of wavefronts arriving at a receiver with different emergence angles. The color code is the same as used for the illustration of the horizontal slowness and emergence angles in Figures 4.14- 4.16, respectively. The angle ϕ can be estimated using equation (4.14).

events from the input shot gather (Figure 4.14(c)): Between 6 and 7 s the ocean bottom can be identified with more or less the same slowness values for both frequencies (marked by blue colors in Figures 4.14(a) and (b)). In the case of muted data or null traces, the horizontal slowness were set to 999 since zeros within the data did not yield reliable slowness values. Those slowness values map as red areas above the ocean bottom reflections (trace muting) or as red vertical traces (null traces). The complete color code for the following figures is: Red colored reflections in the slowness sections are associated with wavefronts arriving with a negative angle at the receiver and consequently the blue colors corresponds to positive emergence angles (measured from the vertical ($\phi = 0°$) to the surface ($\phi = 90°$), see Figure 4.13). Due to the 999 values, the following figures show clipped slowness sections in a range between $-5 \cdot 10^{-4}$ s/m and $5 \cdot 10^{-4}$ s/m.

Between a two-way travel time (TWT) of 7 s and TWT 13 s several events are visible. They appear somewhat more pronounced on the 27 Hz section (larger time windows) but they seem to vanish in the corresponding Fresnel images (Figures 4.14(d) and (e)). At approximately 13 - 14 s a tail from the ocean bottom multiple is visible also weakly appearing on the lowermost part of the depth sections. The difference between the image obtained from the slowness sections for $f_{dom} \approx 27$ Hz and $f_{dom} \approx 42$ Hz seem negligibly small. Also the zooms (Figure 4.14(f)) show nearly identical depth sections.

A quantitative representation of the differences between the slowness sections (Figures 4.14(a) and (a)) and between the corresponding images (Figures 4.14(d)

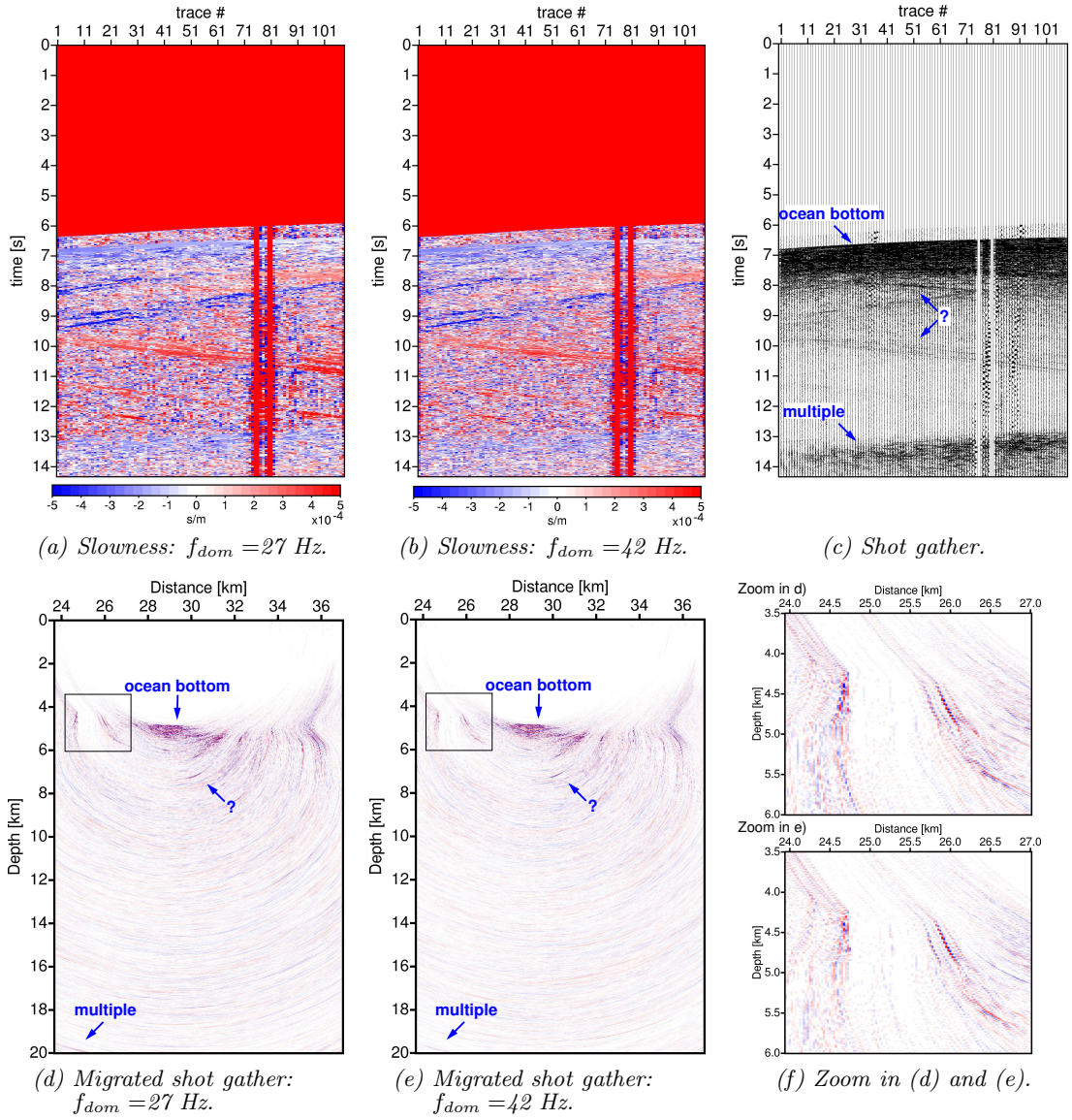

(a) Slowness: f_{dom} =27 Hz. (b) Slowness: f_{dom} =42 Hz. (c) Shot gather.

(d) Migrated shot gather: f_{dom} =27 Hz. (e) Migrated shot gather: f_{dom} =42 Hz. (f) Zoom in (d) and (e).

Figure 4.14: Estimated horizontal slowness from shot no.1761 located at about 29 km along profile for (a) 27 Hz and (b) 42 Hz, respectively. The corresponding shot gather is displayed in Figure 4.14(c). Muted data and null traces map as red areas and respectively red vertical traces in the slowness sections. The lower pictures illustrate the corresponding Fresnel Volume Migration results of this shot. Figure 4.15.

and (e)) can be seen in Figure 4.15. Equal slowness values map as white samples in the difference section (Figure 4.15(a)). Except from the white connected regions below the seafloor almost no coherent event is visible. Also the depth section (Figure 4.15(b)) exhibits only small discrepancies in the vicinity of the ocean bottom images. Thus, the overall impression from the difference sections is that the quality of the

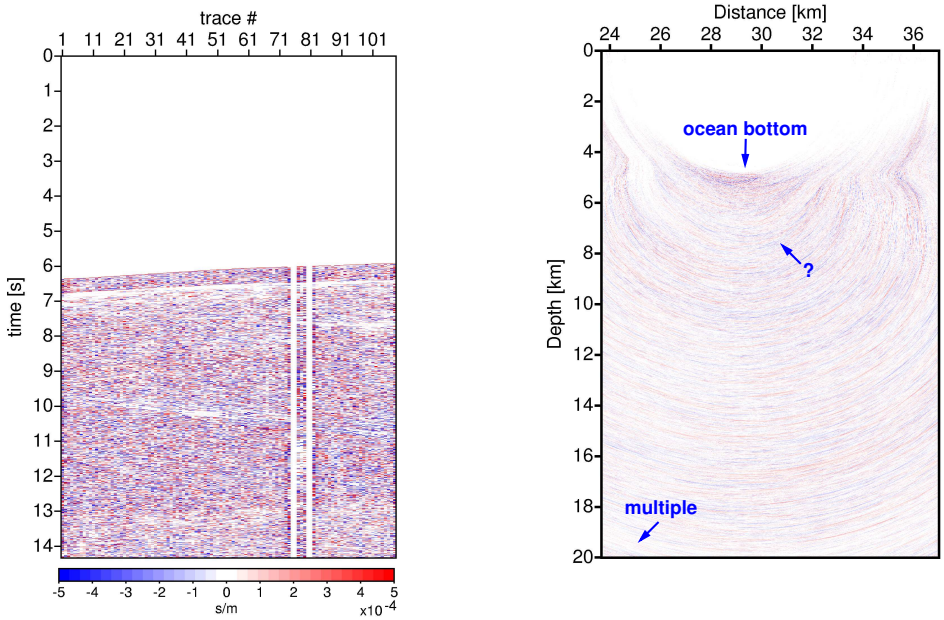

(a) Difference Figure 4.14(b)-Figure 4.14(a).

(b) Difference Figure 4.14(e)-Figure 4.14(d).

Figure 4.15: (a) difference between slowness section Figure 4.14(b) ($f_{dom} \approx 42$ Hz) and Figure 4.14(a) ($f_{dom} \approx 27$ Hz). Samples, where the sections are identical, are colored white. (b) difference between the migrated shot sections Figures 4.14(e) and (d).

results is more or less independent of the choice of the dominant frequency. Nevertheless, the zooms in Figure 4.14(f) show a slightly better image for $f_{dom} \approx 27Hz$. Thus, the latter frequency was used for the slowness calculation in the following.

For line SO104-13, a few examples for the slowness and the related emergence angles are shown in Figures 4.16 and 4.17. The left columns exhibit the common shot gathers (note that the first 3 s are removed) from three different locations: at 3 km (Figure 4.16 top), at 55 km (Figure 4.16 bottom) and at 103 km (Figure 4.17) along the profile. The middle columns contains the corresponding horizontal slowness sections calculated with a dominant frequency of 27 Hz. On the right hand side in both figures, the emergence angle ϕ is depicted. It was calculated with the help of the components of the slowness vector (p_x, p_z) which are connected to the emergence angle in the following form

$$\phi = \arctan\left(\frac{-p_x}{p_z}\right) = \arctan\left(\frac{-p_x}{\sqrt{\frac{1}{v_0^2} - p_x^2}}\right), \tag{4.14}$$

where v_0 is the near surface (water) velocity. The color code of the slowness and angle sections is the same as used for the slowness and angle sections of line SO104-07

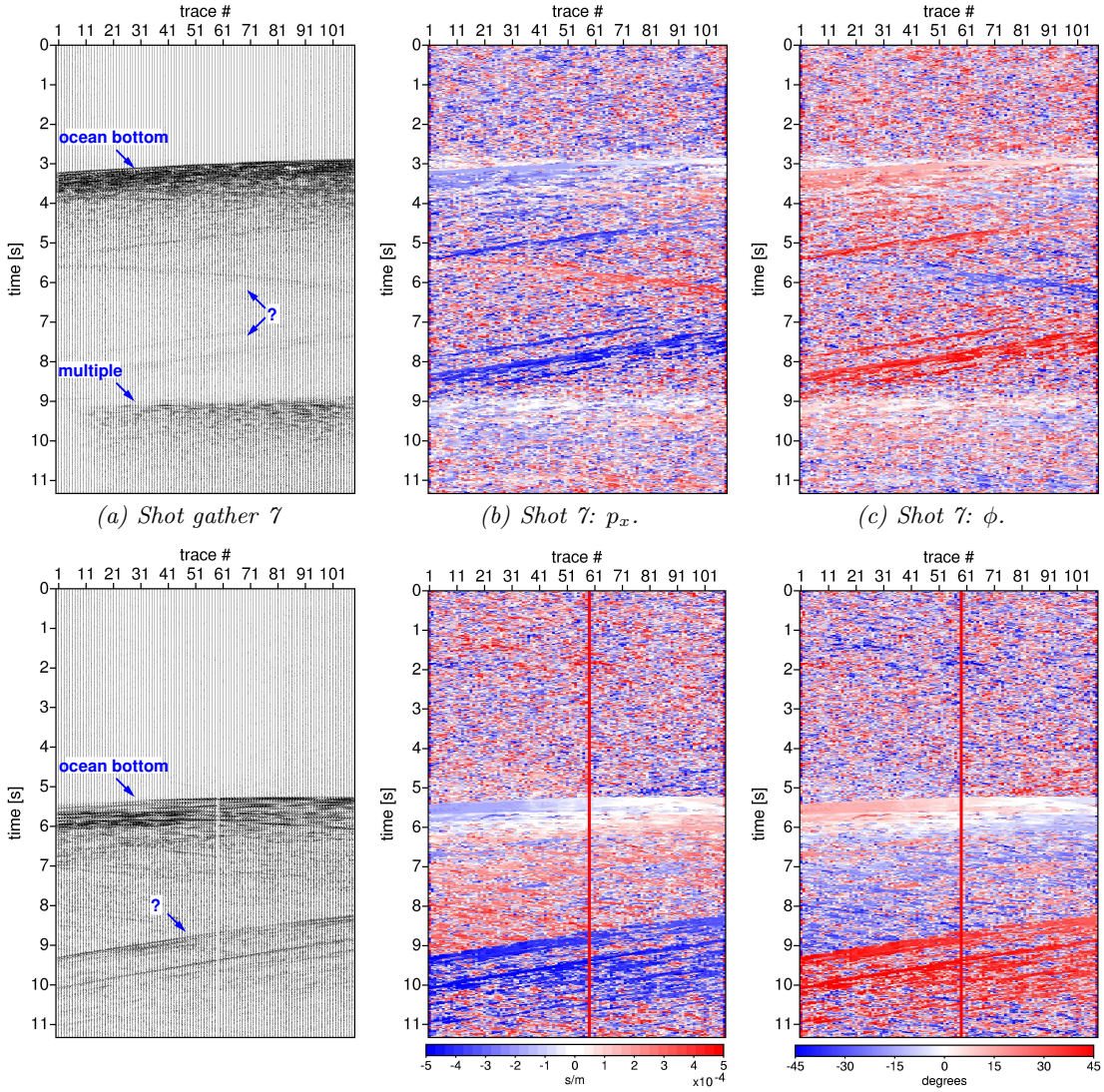

(a) Shot gather 7 *(b) Shot 7: p_x.* *(c) Shot 7: ϕ.*

(d) Shot gather 1032 *(e) Shot 1032: p_x.* *(f) Shot 1032: ϕ.*

Figure 4.16: Shot gathers, slowness sections and corresponding emergence angle sections from the start (at 3 km, Figures 4.16(a)-(c)) and the middle (at 55 km, Figures 4.16(d)-(f)), respectively. The angles were calculated using the components of the slowness vectors p_x and p_z (equation (4.14)). Red vertical traces are related to null traces in the shot gathers.

(Figure 4.13 q.v.).

Within the shot gathers as well as in the slowness and angle sections the seafloor is clearly visible. Some remnants of the ocean bottom multiple can be observed at 3 km and 103 km along profile (Figures 4.16(a)- (c) and Figures 4.17(a)-(c)) although Radon filtering was applied. Most of the events labelled by question marks appear as strong migration smiles in the depth images obtained from Kirchhoff Prestack

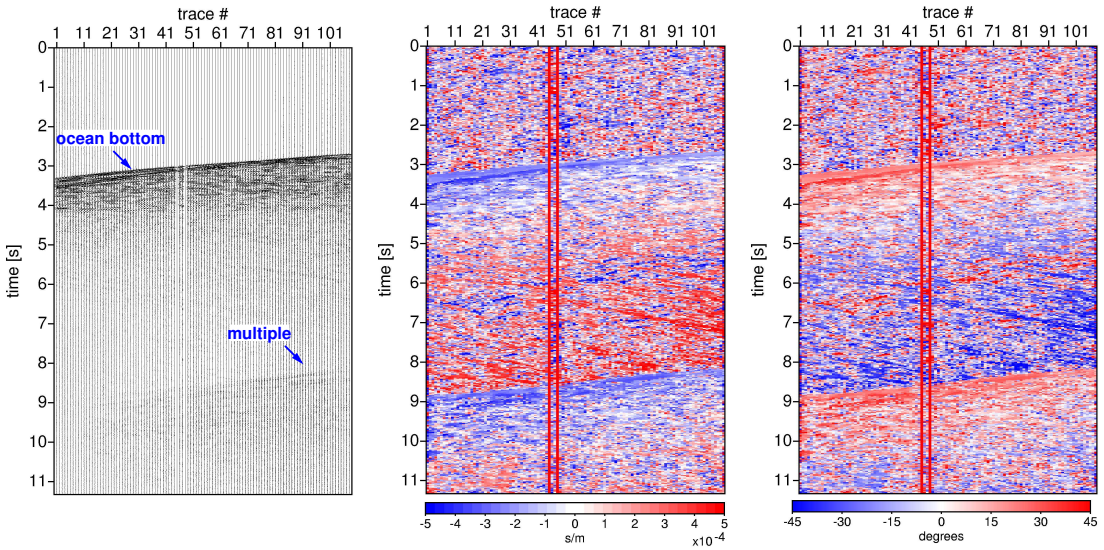

(a) Shot gather 2001 *(b) Shot 2001: p_x.* *(c) Shot 2001: ϕ.*

Figure 4.17: Shot gather, slowness and angle section from the end of line SO104-13 at about 103 km along profile.

Depth Migration which are presented in the next chapter. Especially the shot at 55 km (Figures 4.16(d)-(f)) shows events between 8 s and 10 s which also map on the p_x- and ϕ-sections. This is the region where the ocean bottom exhibits a distinct topography and where the depth images are strongly disturbed by migration artifacts. The results from Fresnel Volume Migration will show that almost all of them will disappear, especially after f-k filtering, except from those which are physically reasonable. This indicates that the migration smiles, at least in this area, are due to the rough ocean bottom topography.

4.6.2 Ray tracing and Fresnel radii estimation

The accomplishment of ray tracing within the migration algorithm is done using a simplification of the paraxial ray approximation (e.g. Beydoun & Keho, 1987; Červený & Soares, 1992 and references therein) for smooth velocity models as proposed by Lüth *et al.* (2005). In general, the ray propagator matrix Π is a 4×4 matrix which contains the second spatial derivatives of the velocity field v (Červený, 2001). At the starting point of the ray the main initial condition is $\Pi \equiv E$, where E is the unity matrix. To avoid numerical problems due to the second derivatives, Lüth *et al.* (2005) supposed a locally constant velocity gradient and neglected the second derivatives. This assumption is acceptable considering that velocity models used for depth migration are in general relatively smooth. Thus, an ordinary differential

equation remains for the required ray propagator element Π_{13}:

$$\frac{d\Pi_{13}}{dt} = v^2 \,. \tag{4.15}$$

Due to the symmetry within the propagator matrix $\Pi_{13} = \Pi_{24}$, the Fresnel zone perpendicular to the ray becomes circular. Besides equation (4.15), two other differential equations have to be solved during the kinematic ray tracing scheme (Červený, 2001). The position vector $\vec{x}$, which describes the particular ray-point coordinates, can be computed using

$$\frac{d\vec{x}}{dt} = v^2\vec{p}, \tag{4.16}$$

and the corresponding slowness vector $\vec{p}$ by

$$\frac{d\vec{p}}{dt} = -\frac{1}{v}\nabla v \,, \tag{4.17}$$

where v is the velocity.

A method to numerically integrate differential equations when the starting parameters are known is provided by the so-called Runge-Kutta method (Butcher, 1987; Hairer *et al.*, 1989). Here, the classical fourth order Runge-Kutta formula was used to calculate the ray coordinates, slowness values as well as the propagator elements at each nodal point Q of the ray

$$\begin{aligned} k_1 &= hf\left(x_n, y_n\right) \\ k_2 &= hf\left(x_n + \frac{1}{2}h, y_n + \frac{1}{2}k_1\right) \\ k_3 &= hf\left(x_n + \frac{1}{2}h, y_n + \frac{1}{2}k_2\right) \\ k_4 &= hf\left(x_n + h, y_n + k_3\right) \\ y_{n+1} &= y_n + \frac{1}{6}k_1 + \frac{1}{3}k_2 + \frac{1}{3}k_3 + \frac{1}{6}k_4 \,. \end{aligned} \tag{4.18}$$

For the ray propagator element (equation (4.15)) and the position vector (equation (4.16)) all of the auxiliary functions $k_i \,, i = 1, \ldots, 4$ in equation (4.18) are coupled with the square of the velocity while for the slowness vector these functions depend on the inverse of the velocity and the spatial derivatives of the velocity field (cf. equation (4.17)). Other terms within equation (4.18) are the ray tracing time step $h(\equiv \Delta t)$ and the total number of ray tracing steps n. With the help of this formula, the required ray propagator element can be calculated. In this case $y \equiv \Pi_{13}$, and the term $f(x_n, y_n)$ is only a function of the square of the velocity (as seen in equation

(4.15)) with the initial condition $\Pi_{13} = 0$ at the starting point of the ray. This means that also the Fresnel radius must be set to zero at the starting point to prevent division by zero in equation (4.11).

However, equation (4.18) shows that the computation time is strongly related to the number of ray tracing steps n and thus to the ray tracing time steps h since they depend on each other. With the help of this numerical method, one ray for each sample of each trace of the raw data was calculated. This implies a careful choice of the parameter h, which equals the time increment for ray tracing (Δt), or similarly of n. In fact, the most reasonable choice might be the sampling rate and the number of samples of the input data but this will result in unacceptable computing time as pictured in Figure 4.18(a). To obtain the correct ray length, the condition '$n \cdot h \equiv n \cdot \Delta t =$ two-way-travel (TWT) time of the considered sample' or similarly $n = TWT/\Delta t$ must be satisfied. Figure 4.18(a) shows the number of ray tracing steps as a function of the sampling rate for a constant two-way-travel time. This is done to find the most useful parameters for an adequate computing time. For the application to real data it is reasonable to assume one of the ray tracing parameters to be constant since the two-way-travel time of each sample of an input trace is different. In the following, the time increment Δt is assumed to be constant while n differs for each sample.

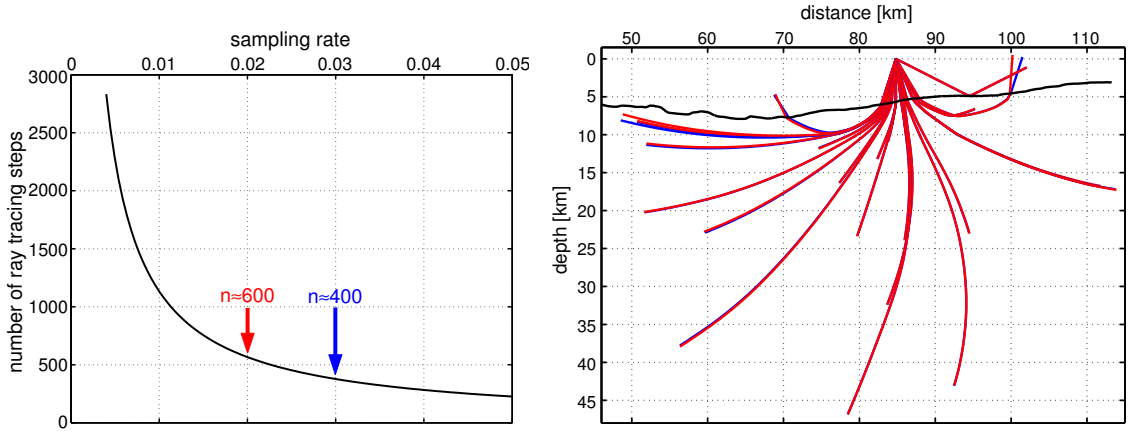

(a) Sampling rate versus number of ray tracing steps.

(b) Rays calculated for two different sampling rates.

Figure 4.18: (a) Number of ray tracing steps needed for varying time increments Δt for a constant two-way-travel time (last sample of the input data). The points marked with the red and blue arrow correspond to the sampling rates used in (b). Figure 4.18(b): Comparison of rays estimated with two different sampling rates. The blue rays were calculated with $\Delta t = 30$ ms which results in approximately 400 ray tracing steps for the last sample (longest ray). A time increment of 20 ms was used for the red rays resulting in about 600 ray tracing steps. The black line marks the ocean bottom.

An example for two time increments is presented in Figure 4.18(b). About 20 rays for different samples of one trace were determined. Thereby, the red and the blue rays were calculated with a time increment of $\Delta t = 20$ ms and $\Delta t = 30$ ms, respectively. The black line illustrates the location of the ocean bottom where a change from water velocity (∼1500 m/s) to about 2800 m/s takes place. This change in velocity is responsible for the abrupt direction change of some rays below the seafloor. At greater depths, it is obvious that the difference between the rays estimated with different sampling rates (time increments) is negligible small compared to the gain of time as the maximum number of ray tracing steps (for the last input sample) increases from about 400 to 600 with decreasing sampling rate (Figure 4.18(a)). Small differences between the rays also means slight variation of the associated Fresnel radii.

Another interesting aspect is the influence of the velocity model roughness on the ray tracing. As discussed above, the approximation by Lüth *et al.* (2005) is strictly valid for smooth velocity models. The cross section of the IFM-model (blue line in Figure 4.19(a)) shows several small steps directly below the seafloor. To avoid large gradients, the model was smoothed (Figure 4.19(a) red line) by averaging the velocity in z-direction by

$$v(x,z) = \frac{v(x,z-1) + v(x,z+1)}{2}\,. \tag{4.19}$$

Figure 4.19 emphasizes the differences between the outcomes of both models by

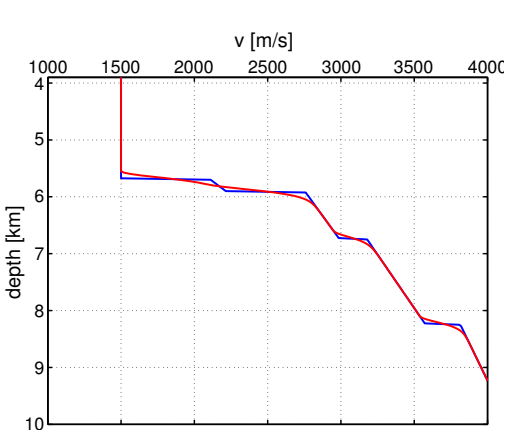

(a) Upper part of the cross section of the IFM-model at about 85 km.

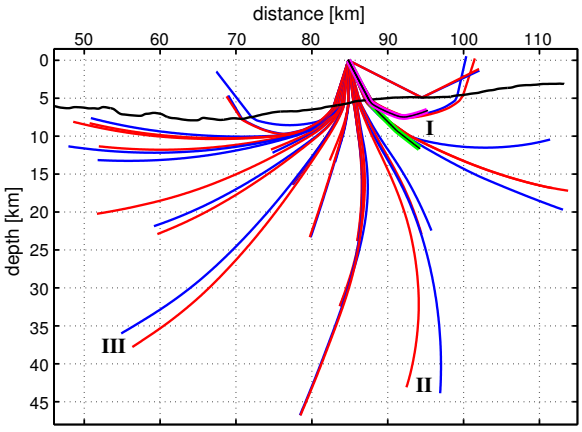

(b) Rays calculated with the IFM-model and a smoothed velocity model.

Figure 4.19: (a) original IFM-model (blue) and the smoothed model (red) in a depth range between 4 km and 10 km. (b) ray tracing results for both models where the color code is the same as in (a). The rays marked by 'I', 'II' and 'III' are separately shown and discussed in the next figure.

means of a few rays. The smoothing procedure generates some distinctive features:

- The principal ray trajectories of nearly all rays are similar compared that oba tined from the IFM-model.
- Due to smoothing, the change from water velocity to a velocity of about $2800 m/s$ takes place at shallower depth (Figure 4.19(a)).
- Strong alterations in ray direction (e.g. green and magenta ray in Figure 4.19(b) marked by 'I') result from the discretization (the time increment in equation (4.18)) and from the different derivatives of the velocities after averaging.
- This alterations can also be a result of different incidence angles (compared to the IFM-model) at the seafloor or at a possible interface within the sedimentary layers.

The impact of velocity smoothing to the Fresnel volumes is pictured in Figure 4.20. Here, the gray curves represent parts of the isochrons which belong to the rays calculated with the IFM-model (blue) and respectively with the smoothed model (red) where rays, labelled with 'I', 'II' and 'III', correspond to the rays with the same label in Figure 4.19).

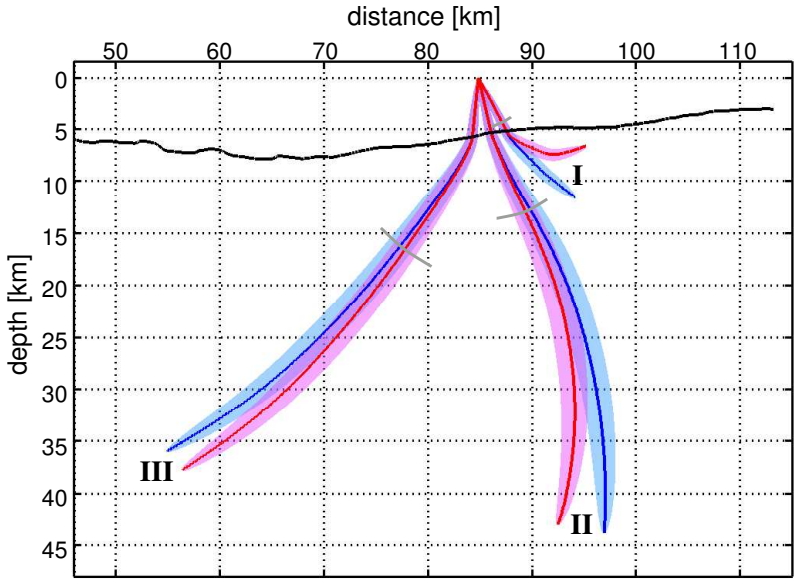

Figure 4.20: Fresnel volumes estimated for three different rays (I, II and III; see also Figure 4.19) with the IFM-model (blue) and the smoothed model (red), respectively. The gray lines are parts of the corresponding isochrons.

For early arriving data samples it is of no importance whether the velocity model is smoothed or not since the isochrons are located above the ocean bottom where the rays coincide. At greater depth, the discrepancy of some rays increases as well as that of the respective Fresnel zones, and correspondingly on where the isochrons intersect the rays.

To point out the effect of smoothing to the imaging results a part of line SO104-13 was migrated using both velocity fields. Figure 4.21(a) illustrates the resulting image of the area between 47 km and 59 km along profile migrated with the IFM-model. The upper right picture (Figure 4.21(b)) shows the result corresponding to the

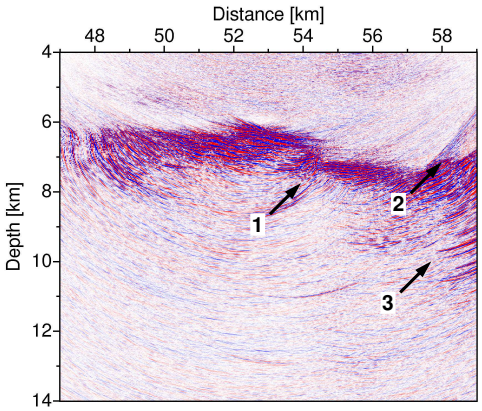

(a) Migrated with the IFM-model.

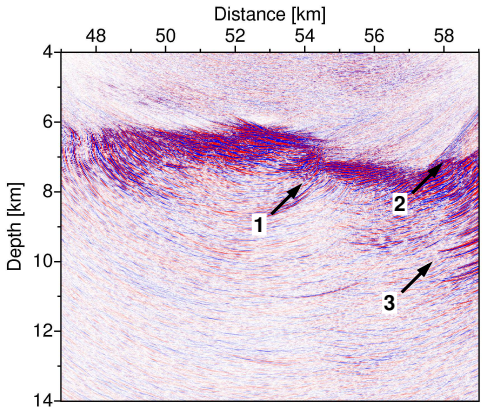

(b) Migrated with a five times smoothed model.

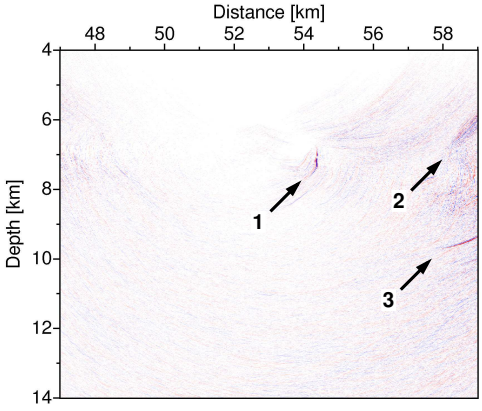

(c) Difference between (a) and (b).

Figure 4.21: Part of the image of line SO104-13 computed for two slightly different velocity models. Figure 4.21(a) illustrates the results from 47 km to 59 km along profile in a depth range between 4 km and 14 km migrated with the IFM-model. The upper right picture shows the section migrated with the smoothed model. The numbered arrows mark that parts of the images where the differences are most obvious. To point out the latter, a difference section is separately shown in Figure 4.21(c).

smoothed model. Numbered arrows mark those portions which comprise the most significant differences between the images. These differences are separately displayed in Figure 4.21(c). The most obvious and maybe the most important discrepancy for interpretation is the vertical reflection event directly below the seafloor (1) which is indeed only visible on the difference section (Figure 4.21(c)). The other two maxima on this section correspond to artifacts resulting from head waves (2) and to an event whose origin is not totally understood. However, only small errors due to smoothing can be observed in Figure 4.21(c). A possible explanation for this relatively small error might be given by the use of a migration operator which is tapered at the boundary of the first Fresnel zone (equation (4.9)). Thus, the smoothed version of the velocity models were used for the complete data sets. This is done to avoid numerical problems during ray tracing.

As mentioned above, the used ray tracing formalism works with the help of the virtual source point method and not with a two point ray tracing technique, since the locations of possible reflectors at depth are unknown. Due to the increasing velocity with depth (below the seafloor), the virtual source point method may lead to rays which are too long. For a given two-way-travel time, the distances between the ray nodes of the corresponding ray increase with increasing velocity. This leads to an overestimation of the Fresnel volumes and thus of the required Fresnel zone. Thus, the restriction of the migration operator in form of the weighting function is not quite correct since additional signal from outside the actual Fresnel zones is included into the summation process. As the vertical velocity gradient has no influence on the location of the ray, the center of the Fresnel zones is correctly estimated. The use of a linear taper at the boundaries of Fresnel volumes might compensate the effect of overestimated Fresnel volumes. Even though the Fresnel zones were estimated slightly wrong, a significant improvement of the images compared to the Kirchhoff Prestack Depth Migration results indicate a negligible influence of the overestimation of the Fresnel volumes on the migration results.

4.6.3 Fresnel Volume Migration

Apart from ray tracing, the key step of the Fresnel Volume Migration routine is the computation of the Fresnel weight (equation (4.12)) and the exact use of it. If a single trace of the data set is considered, the first step within the migration routine is to extract the two-way-travel time for each image point in the subsurface from the travel time tables. For each particular image point, that ray has to be found which is associated with the corresponding isochron. Then, the closest ray node of this image point has to be determined. The distance between these two points is then compared with the Fresnel radius at the respective ray point. Figure 4.22

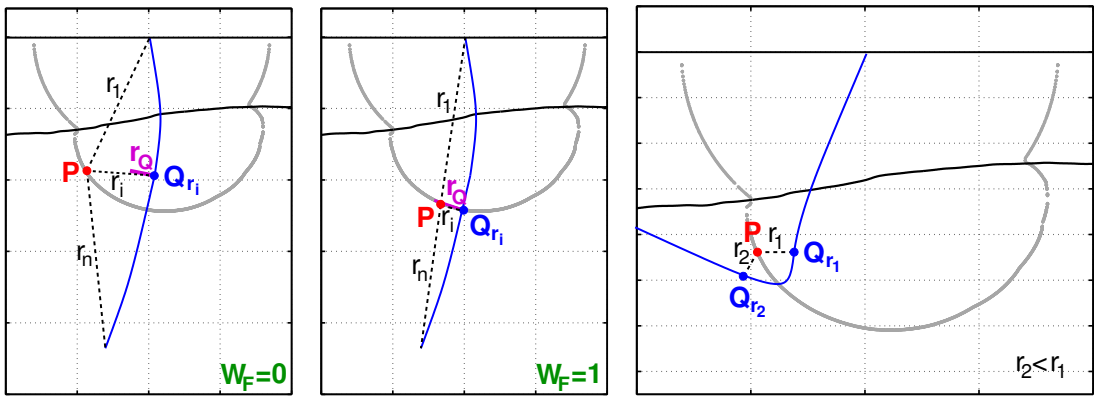

(a) $r_i > 2r_Q$ (b) $r_i \leq r_Q$ (c) *A complex ray trajectory can lead to inaccuracies when the routine stops at the first local minimum.*

Figure 4.22: (a) and (b) describe the process to determine the closest of the n ray nodes Q for an arbitrary image point P. The weighting factor W_F is zero if $r_i > 2r_Q$ ((a)) and $W_F = 1$ for $r_1 \leq r_Q$ ((b)). For $r_Q < r_i \leq 2r_Q$, W_F is linearly tapered. An example for an extremely curved ray is shown in Figure 4.22(c). Here, $r_1 > r_2$ which may lead to an error if P is located within the second Fresnel zone of Q_{r_2} but outside of that of Q_{r_1} when the process stops at the first minimum (r_1).

demonstrates this procedure. Consider an arbitrary subsurface point P and the ray with the corresponding two-way-travel time. The first step is to calculate the distances r to all n ray points Q, starting with r_1 (dashed black lines). The value of the weighting factor W_F depends on whether the minimum distance r_i is greater than the second Fresnel radius $2r_Q$ or not (the first Fresnel radius is depicted as a solid magenta line in Figure 4.22). It is one if, and only if $r_i \leq r_Q$ (Figure 4.22(b)) and it becomes zero when $r_i > r_Q$ (Figure 4.22(a)). In the case $r_Q < r_i \leq 2r_Q$ the weighting factor is linearly tapered (equation (4.12)). This weight is then applied to the amplitude of the trace with the same two-way-travel time.

It is clear that both, searching for the minimum distances between image and ray points and comparing it with the Fresnel radii are the most time-consuming processes within the algorithm. To speed up the program, a criterion was integrated which stops the searching process after the first local minimum has been found. This minimum is defined as that distance between P and ray node Q (r_i in Figures 4.22(a) and (b)) where the previous distance (r_{i-1}) and the following distance (r_{i+1}) are greater but, however, there might be a value for a deeper ray node which is smaller than the local minimum (global minimum). This can be done by assuming that the rays are not extremely curved. Figure 4.22(c) shows an example for a ray with a complex trajectory. Here, the first local minimum r_1 is not equal to the global minimum (r_2). In this case, where r_1 is assumed to be larger than the second Fresnel

radius of ray point Q_{r_1} but P is located inside the second Fresnel zone of point Q_{r_2}, the amplitude value of the related sample is wrongly multiplied by zero during the summation. For the CINCA data sets this case is extremely rare to absent so that the limitation of the searching procedure did not lead to significant errors.

A complete insight into what is done during Fresnel Volume Migration is displayed in Figure 4.11. The summary of the results from each step in form of four rays with the corresponding Fresnel volumes, isochrons and image points within the Fresnel zones as well as the illustration of the effect of reduction of the computational time due to the local minimum approach is pictured in Figure 4.23. Thereby, light-colored red areas correspond to the Fresnel volumes when the complete ray is scanned during the searching algorithm whereas the blue colored areas represents the local minimum approach. As in the further pictures, the isochrons are colored gray. Only the green image points on the isochrons contribute to the resulting migrated images.

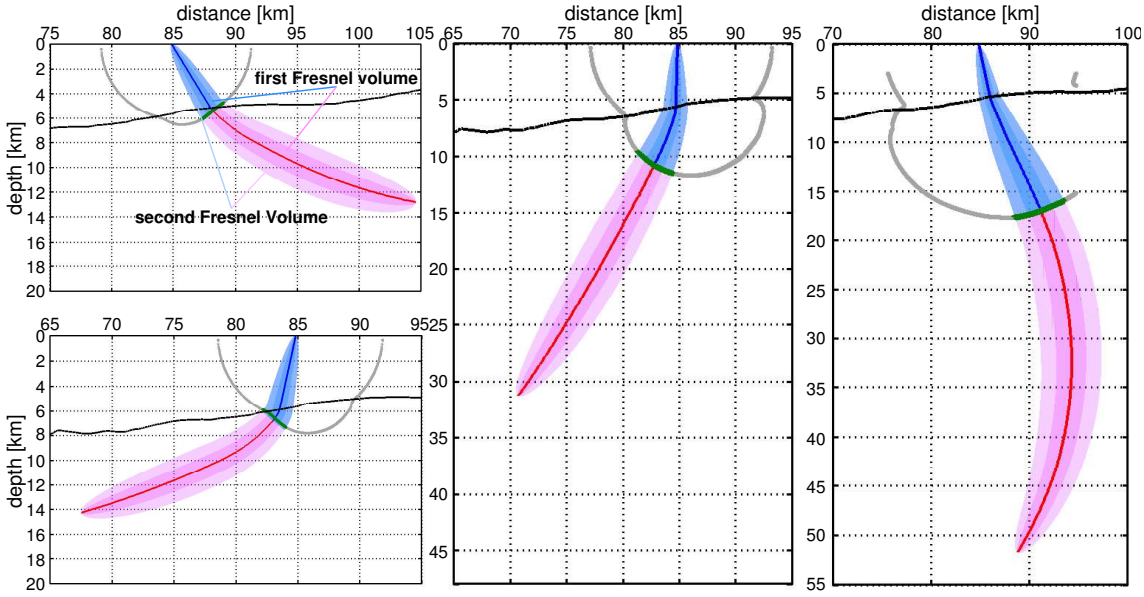

Figure 4.23: The light-colored red areas correspond to the complete Fresnel volumes of the rays. The here presented approximation only searches the blue part of the ray and it stops when the first local minimum is reached. The green parts of the isochrons (gray lines) depict the image points located inside the second Fresnel volumes.

For the complete data sets, all this is done for all traces (with approximately 3000 samples each), shot gather by shot gather, and at last all migrated single shot sections were stacked to get a complete depth image along the profile.

4.7 Summary and discussion

In this chapter the evolution of the Fresnel Volume Migration approach from the Kirchhoff Prestack Depth Migration was introduced. The travel time calculation was done using two different velocity models: The IFM-model as an extension of an existing velocity field of the outer forearc and the wide-angle model constructed with the information about the seismic boundaries from wide-angle seismics. Thereby, the main differences between the models appear west of the trench where the IFM-model contains maximum velocity values of about 5500 m/s and the wide-angle model velocities up to 8500 m/s. These values indicate too low velocities within the IFM-models as expected for the oceanic crust. To the east of the trench these differences decrease. It is clear, that an inaccuracy of the location of the seismic boundaries complicated an exact modelling of the velocity field. A discussion of the influence of the different velocity fields to the migration results is given in the next chapter.

Additionally to the introduction of the Fresnel Volume Migration, a study with respect to some of the input parameter was accomplished. The cross-correlation method was used to calculate the horizontal slowness sections. The most important input parameters for these calculation scheme are the spatial and temporal window size necessary to find the time shifts associated with the most coherent signal. While temporal length is a function of the dominant frequency, the spatial extent depends on the dominant wavelength. Heigel (2005) proposed the use of four traces around the reference trace for the spatial window length.

A spectral analysis was performed to extract the dominant frequency for some representative shot gathers of line SO104-07 as well as of line SO104-13. The power spectrum of a shot of line SO104-13 showed a clear peak at about 27 Hz. In contrast, the spectrum obtained from line SO104-07 comprised at least two maxima. A comparison of the migration results obtained with slowness sections calculated with 27 Hz and respectively with 42 Hz indicated slightly better depth images for a dominant frequency of 27 Hz.

The ray tracing algorithm requires several input parameters. Most important with respect to the computing time are the sampling rate and the number steps during the ray tracing. A sufficient condition for the choice of these parameters is that their product equals the two-way-travel time of the respective sample of the input data to obtain the exact ray length. This implies, that the most reasonable values might be the sampling rate and the number of samples of the input data but it has been shown that this choice would result in unacceptable computing time. It has to be considered, that these input parameters are also sensitive to the roughness of the

used velocity model since abrupt velocity changes can lead to problems with the ray directions along the interfaces. A test of several different sampling rates resulted in rays which showed negligible small differences. Thus a sampling rate of $dt = 30$ ms were chosen resulting in a maximum of 400 ray tracing steps.

The influence of velocity smoothing was demonstrated and discussed. Obvious changes of the ray trajectories below the seafloor have been observed after smoothing. Consequently, this change in direction led to slightly different Fresnel volumes. Fresnel Volume Migration were carried out with both, the original IFM-model and a fife times smoothed version of the IFM-model. The resulting depth sections offered quite similar images. This indicated that the tapering at the boundaries of the first Fresnel volumes compensated for the effects due to smoothing so that slightly different estimates of the Fresnel zones did not significantly influence the migration results.

A method was proposed to decrease the computing time which stops the searching process within the Fresnel Volume Migration when the first local minimum distance between image point and ray node is reached. The assumption that no extremely curved rays appear is supported by the fact that the velocity models are build up of only smooth velocity gradients in each direction. The application of this local minimum criterion resulted in a significant decrease of computing time.